

This preprint is for a manuscript submitted for publication in Remote Sensing of Environment. Note that the content may change somewhat in subsequent versions of the manuscript. Please feel free to contact any of the authors if you have any feedback or suggestions.

On the Land Emissivity Assumption and Landsat-Derived Surface Urban Heat Islands: A Global Analysis

TC Chakraborty¹

Yale School of the Environment

Xuhui Lee

Yale School of the Environment

Sofia Ermida

Instituto Portugues do Mar e da Atmosfera

Wenfeng Zhan

Nanjing University

Abstract

The prescription of surface emissivity (ε) strongly controls satellite-derived estimates of land surface temperature (LST). This is particularly important for studying surface urban heat islands (SUHI) since built-up and natural landscapes are known to have distinct ε values. Given the small signal associated with the SUHI compared to LST, accurately prescribing urban and rural ε would improve our satellite-derived SUHI estimates. Here we test the sensitivity of SUHI to the ε assumption made while deriving Landsat LST for almost 10,000 global urban clusters for summer and winter days. We find that adjusting the ε values from the Advanced Spaceborne Thermal Emission and Reflection Radiometer (ASTER) dataset based on pixel-level normalized difference vegetation index (NDVI) improves our ability to capture the summer to winter contrast in SUHI. Overall, the difference between the two methods is moderate; around 10% during summer and around 20% during winter, though this difference varies by

¹Corresponding Author: tc.chakraborty@yale.edu

climate zone, showing higher deviations in polar and temperate climate. Using both methods of prescribing ε , we provide the first global estimates of SUHI derived from Landsat. During summer, the global mean SUHI varies between 2.31 °C (0.24 °C for winter) when using ASTER ε to 2.54 °C (0.29 °C for winter) after NDVI-adjustment. Compared to Moderate Resolution Imaging Spectroradiometer (MODIS) Terra observations, Landsat data show higher SUHI daytime intensities during summer (by more than 1.5 °C), primarily due to its ability to better resolve urban pixels. We also find that the ε values prescribed for urban land cover in global and regional weather models are lower than the satellite-derived broadband ε values. Based on the sensitivities to ε we find for urban and rural LST, this would imply overestimation of SUHI by these models (by around 4 °C for both summer and winter), all else remaining constant. Our analysis provides a global perspective on the importance of better constraining urban ε for comparing satellite-derived and model-simulated urban heat islands. Since both the structural and geometric heterogeneity of urban areas controls the bulk ε , future studies should try to benchmark the suitability of existing LST- ε separation methods over urban areas.

Keywords: Land Surface Temperature, Urban Heat Island, Surface emissivity, Landsat, MODIS, Global, Google Earth Engine

1. Introduction

The physical process of urbanization involves replacement of natural landscapes with built-up structures, modifying the biophysical properties of the land surface (Carlson and Arthur, 2000). One major and widely studied consequence
5 of urbanization is the urban heat island (UHI) effect. The UHI is the usually positive temperature difference between the urban area and a non-urban reference, essentially isolating the impact of urbanization on local temperature (Oke, 1969, 1982; Arnfield, 2003). The UHI can contribute to urban heat stress, enhance energy demand for cooling, and may impact local-scale cloud cover and
10 rainfall (Arnfield, 2003; Shastri et al., 2015; Li et al., 2019; Theeuwes et al.,

2019).

Traditionally, the UHI has been quantified as the difference in near-surface air temperature (AT) between the urban core and a rural reference (Voogt, 2007). Since urban areas can have large heterogeneity, it can be difficult to
15 capture a representative value of urban temperature using standard weather stations (Stewart, 2011). Moreover, dense meteorological networks, which are rarely available over cities (Muller et al., 2013), are necessary to capture the intra-urban temperature variability, which has implications for disparities in heat exposure (Chakraborty et al., 2019a). The advent of satellite observa-
20 tions in the thermal infrared (TIR) channels has allowed researchers to remotely measure the land surface temperature (LST) over urban areas (Rao, 1972). Although LST and AT are not physically identical quantities, it is easier to estimate intra-urban variability in LST from satellites due to their spatially explicit coverage. The global availability of some of these LST products has also en-
25 abled multi-city comparisons that are difficult using ground-based observations (Peng et al., 2011; Clinton and Gong, 2013; Chakraborty and Lee, 2019). The UHI derived using satellite data is commonly referred to as surface UHI (SUHI), while traditional weather station-based UHI estimates are known as canopy UHI (CUHI) (Bonafoni et al., 2015; Chakraborty et al., 2016).

30 Although satellite-based LST has several advantages over ground-based observations of AT, it is a derived quantity whose accuracy depends on several factors (Dash et al., 2002). Satellites measure the top of the atmosphere thermal radiance (L_{toa}), which can be approximated as:

$$L_{toa} = \tau L_{surf} + L_{u,atm} + L_{d,atm}(1 - \varepsilon)\tau \quad (1)$$

Here ε is the surface emissivity, τ is the atmospheric transmissivity, L_{surf} is
35 the surface emission of thermal radiation, and $L_{u,atm}$ and $L_{d,atm}$ are the upward and downward components of the thermal radiation emitted by the bulk atmosphere. All of these variables are wavelength dependent. The measured L_{toa} is then combined with multiple ancillary data to compute L_{surf} , which can then

be inverted to estimate LST from an approximation of the Stefan–Boltzmann
40 law:

$$L_{\text{surf}} = \varepsilon\sigma\text{LST}^4 \quad (2)$$

where σ is the Stefan–Boltzmann constant ($5.67 \times 10^{-8} \text{ W m}^{-2} \text{ K}^{-4}$). The values of τ , $L_{\text{u,atm}}$, and $L_{\text{d,atm}}$ are dependent on atmospheric conditions and may be obtained from radiative transfer models. On the other hand, ε - a spectrally varying ratio of emitted radiation of a material compared to the
45 radiation of a black body at a particular temperature - is primarily a property of the land surface (Li et al., 2013b).

Since both ε and LST determine L_{surf} , as per Eq. 2, estimates of ε are a prerequisite for accurately calculating LST. Unfortunately, even if the atmospheric properties that influence τ , $L_{\text{u,atm}}$, and $L_{\text{d,atm}}$ are perfectly known, ε and LST
50 cannot be analytically separated from satellite observations (Hook et al., 1992; Dash et al., 2002; Li et al., 2013a). Conceptually, for TIR measurements in n channels, we get n equations (one for each channel) for $n+1$ unknowns (ε for n channels and LST). As such, several empirical methods are used to determine ε . The first is a temperature emissivity separation (TES) method that solves
55 the n equations with an additional empirical constraint to equalize the number of equations and unknowns (Gillespie et al., 1998). Another is an NDVI-based emissivity method (NBEM), where different thresholds of normalized difference vegetation index (NDVI), a proxy for live green surface vegetation, are used to specify the emissivity (Van De Griend and Owe, 1993; Valor and Caselles,
60 1996). Finally, there are classification-based emissivity methods (CBEM), with each land cover prescribed a value based on look-up tables (Snyder et al., 1998). Each method has its advantages and disadvantages and the choice of method is of particular concern when studying the SUHI (Mohamed et al., 2017). Although the vast majority of studies that use the derived LST products from Moderate
65 Resolution Imaging Spectroradiometer (MODIS) observations implicitly use a CBEM method, there is less agreement on the method used to estimate LST from Landsat observations in the scientific literature. Regardless of the method

used, specifications of ε lead to some of the largest uncertainties in satellite-derived LST (Jiménez-Muñoz and Sobrino, 2003).

70 The challenge of accurately prescribing ε is particularly difficult for urban areas (Artis and Carnahan, 1982; Mohamed et al., 2017). Real urban areas vary widely in material composition of the built-up structures, varying presence of other land cover types like vegetation, barren soil, and undeveloped land, as well as large differences in surface geometry that can also influence bulk ε
75 (Voogt and Oke, 1998; Mitraka et al., 2012; Quan et al., 2016). A single value for urban ε , which is frequently used in many CBEM methods, is simplistic since the different materials used in urban construction have widely different ε (Marshall, 1982; Chen et al., 2016). Also, NBEM methods are affected by this uncertainty since NDVI-based threshold cannot explicitly account for differences
80 in the built-up structures and surface geometry across cities. Even within cities, different materials, and thus different ε values, are common, with potential impacts on estimating intra-urban LST variability from higher resolution satellite observations, such as from Landsat (Artis and Carnahan, 1982). TES methods, although conceptually the most accurate, are influenced by the relatively
85 higher uncertainties in satellite observations over urban areas due to multiple factors, from urban heterogeneity to thermal anisotropy (Lagouarde et al., 2004; Hu et al., 2016). Moreover, this method requires observations in several TIR channels.

Previous studies on the importance of ε on urban LST have primarily focused
90 on the overall ε of individual cities (Chen et al., 2016; Mohamed et al., 2017), not the urban-rural differential in ε ($\Delta\varepsilon$) and how that might impact the computed SUHI for global urban areas. The method of estimating $\Delta\varepsilon$ would affect the SUHI estimate even when the emitted thermal differential between urban and rural areas is held constant, since urban areas are known to have a distinct
95 ε from most natural surfaces (Sobrino et al., 2012; Yang et al., 2015). The $\Delta\varepsilon$ would also vary across different cities since both the typology of building materials (Voogt and Oke, 2003) and the land cover of the rural reference vary (Van De Griend and Owe, 1993; Zhao et al., 2014). The combined impact of

these two sources of variability in ε on SUHI estimates across cities has not been
100 studied in the past. The influence of $\Delta\varepsilon$ on SUHI estimates is also important
for regional and global land models. Land models have improved from using
broadband ε of 1 for all land surfaces in old global models (Sellers et al., 1986) to
using land cover specific prescribed ε in more recent implementations (Jin and
Liang, 2006; Chakraborty et al., 2019b). The use of prescribed ε is of particular
105 concern for urban modeling studies due to the lack of observational constraints
on this parameter as well as the large differences seen between prescribed and
measured ε (Li et al., 2017).

Here we attempt to comprehensively examine the impact of the ε assumption
on estimates of Landsat-derived SUHI both globally and across broad climate
110 classes. Our goal is to add to the recent studies that have investigated the
influence of the methods used while calculating the SUHI - including choice of
temporal composites and LST products (Hu and Brunsell, 2013; Chakraborty
et al., 2020; Yao et al., 2020), as well as definitions of the non-urban reference
(Chakraborty and Lee, 2019; Zhang et al., 2019; Chakraborty et al., 2020) - with
115 a focus on the fundamental derivation of LST from satellite measures of thermal
surface emissivity. We also use this opportunity to provide the first global
estimates of daytime SUHI using Landsat observations for two different methods
of ε prescription and discuss their potential applications and limitations when
compared to more commonly used MODIS-derived values. Finally, to provide
120 an integrated perspective on future research directions in urban climatology, we
discuss the implications of the prescribed ε in modeled SUHI estimates when
compared to satellite-derived ‘observations’.

2. Material and methods

2.1. Deriving land surface temperature

125 Here we estimated global LST by combining top of the atmosphere bright-
ness temperature (T_b) data and a vegetation index derived from the Landsat 5
satellite (Loveland and Dwyer, 2012) and ε estimates from the Advanced Space-

borne Thermal Emission and Reflection Radiometer (ASTER) sensor (Abrams, 2000). The Landsat 5 satellite orbited the Earth in a sun-synchronous, near-
130 polar orbit and had a 16-day repeat cycle with an equatorial crossing time of around 9:45 am local time. The satellite observed the Earth in 7 channels, with all but the TIR channel (10.4 - 12.5 μm ; 120 m native resolution) having a native resolution of 30 m. Data from Landsat 5 are available from 1984 to 2012. ASTER is a multi-spectral imaging instrument on board the Terra satellite,
135 which has a sun-synchronous orbit and crosses the equator at roughly 10:30 am local time. ASTER and its subsystems have been imaging the Earth’s surface in 14 channels with a repeat cycle of 16 days since the year 2000. The resolution varies from 15 m for the VNIR (Visible and Near-Infrared) bands to 30 m for the SWIR (ShortWave Infrared) bands to 90 m for its 5 TIR channels (8.125
140 - 8.475 μm , 8.475-8.825 μm , 8.925-9.275 μm , 10.25-10.95 μm , and 10.95-11.65 μm).

Since T_b and LST are non-linearly related and all terms of Eq. 1 are not known for every pixel, generalized models used to estimate LST from satellite observations usually linearize the radiative transfer equation, which includes
145 both a linearization of the Planck’s function and contributions from atmospheric interference. Here we use the Statistical Mono-Window (SMW) algorithm as implemented by Ermida et al. (2020) on the Google Earth Engine (GEE) platform (Gorelick et al., 2017) to compute LST. The SMW algorithm represents LST as a linear function of prescribed ε and the Landsat-observed T_b (Duguay-Tetzlaff
150 et al., 2015) and is given by:

$$\text{LST} = A_i \frac{Tb}{\varepsilon} + B_i \frac{1}{\varepsilon} + C_i \quad (3)$$

Here the coefficients of the equation for Landsat band i (A_i , B_i , and C_i) were derived from radiative transfer simulations for 10 classes of Total Column Water Vapour (TCWV). For more information about the calibration procedure used to estimate these coefficients, please see Ermida et al. (2020).

155 *2.2. Surface Emissivity for Land Surface Temperature Estimation*

Equation 3 is a function of prescribed ε , which is estimated using two methods - the TES method used to generate the ASTER Global Emissivity Database version 3 (ASTER GEDv3) and a NBEM approach. The ASTER GEDv3 dataset was developed by the the National Aeronautics and Space Administration's (NASA) Jet Propulsion Laboratory (JPL) from clear-sky ASTER images
 160 between 2000 and 2008 (Hulley et al., 2015). The data are available at a resolution of 100 m for all 5 of ASTER's TIR channels. These data can be directly used in Eq. 3 after adjusting to the Landsat TIR band using the equation described in Malakar et al. (2018):

$$\varepsilon_{10.40-12.5} = c_{13}\varepsilon_{13} + c_{14}\varepsilon_{14} + c \quad (4)$$

165 Here $\varepsilon_{10.40-12.5}$ corresponds to the ε for the Landsat 5 TIR channel, ε_{13} and ε_{14} correspond to band 13 (10.25-10.95 μm) and 14 (10.95-11.65 μm) of the ASTER GEDv3 dataset, and c , c_{13} , c_{14} are empirical regression coefficients. For Landsat 5, these coefficients equal 0.0195, -0.0723, and 1.0521, respectively (Malakar et al., 2018).

170 For the NBEM approach, the actual ε for each pixel was computed by adjusting the mean ε in the ASTER GEDv3 by the fractional vegetation cover (FVC) estimated from the corresponding Landsat 5 data (Ermida et al., 2020). The FVC can be computed using the relationship from Carlson and Ripley (1997):

$$\text{FVC} = \left[\frac{\text{NDVI} - \text{NDVI}_{\text{bare}}}{\text{NDVI}_{\text{veg}} - \text{NDVI}_{\text{bare}}} \right]^2 \quad (5)$$

175 Here NDVI is derived from the surface reflectances in the Near Infrared (NIR; 0.78-0.86 μm for ASTER and 0.77-0.9 μm for Landsat 5) and RED (0.63-0.69 μm) bands. $\text{NDVI}_{\text{bare}}$ and NDVI_{veg} are the reference NDVI for completely bare and completely vegetated pixels, respectively. $\text{NDVI}_{\text{bare}}$ is set as 0.2 and NDVI_{veg} is equal to 0.86 based on previous estimates (Tang et al., 2010; Wang et al., 2015; Ren et al., 2017). The NDVI-adjusted ε was then calculated using
 180 the equation:

$$\varepsilon = \text{FVC}\varepsilon_{\text{veg}} + (1 - \text{FVC})\varepsilon_{\text{bare}} \quad (6)$$

Equation 6 is wavelength dependent, but for the Landsat 5 TIR band, ε_{veg} was set to 0.99 due to the small variability for vegetated surfaces (Peres and DaCamara, 2005), while $\varepsilon_{\text{bare}}$ is estimated from ASTER measurements (Ermida et al., 2020).

185 In addition to these methods that consider spatial variability in ε , we also modified the open-source GEE module (Ermida et al., 2020) to calculate global LST for different prescribed values of ε from 0.88 to 1 with a step size of 0.02. This was done as a perturbation analysis to test the sensitivity of the LST derived for both urban and rural surfaces from the SMW algorithm.

190 Both to minimize computational costs and since the overall focus was the impact of different values of ε on urban and rural LST, we used a single year (2010) of Landsat 5 data for the analysis. In the present study, the data used for estimation of ε , NDVI, and LST were first screened using cloud masking algorithms. For the NIR and RED bands, used to compute NDVI, both clouds
 195 and cloud shadows were removed based on the pixel-level quality flags. For TIR, only pixels with no cloud contamination were considered. Since different regions of the world can have different amounts and even seasonality of cloud cover, we attempted to minimize the impact of this inter-regional variability by focusing on summer and winter separately rather than annual means. Summers
 200 are defined as the months of June, July, and August in northern hemisphere and December, January, and February in the southern hemisphere, and vice versa for winter. This is consistent with the practice of separately studying the SUHI for summer and winter in the literature (Peng et al., 2011; Clinton and Gong, 2013; Chakraborty and Lee, 2019). Overall, based on this temporal subsetting,
 205 each pixel can have a maximum of 5 to 6 Landsat observations during the study period.

2.3. Estimating Surface Urban Heat Islands

To estimate the SUHI, we calculated the LST for pairs of urban and rural references for each of almost 10,000 urban agglomerations or clusters (Fig. 1a) that form the base of the Yale Center for Earth Observation (YCEO) Global Surface UHI Dataset (Chakraborty and Lee, 2019). The original urban boundaries are based on global urban extent data derived from MODIS (Schneider et al., 2010). Note that the vast majority ($\approx 89\%$) of these clusters are in the northern hemisphere. We checked whether Landsat provides representative observations over the urban clusters after pixel-level cloud screening. Figure 1b shows the percentage of the maximum possible pixels in each cluster with at least one observation from Landsat during northern hemisphere summer. Overall, after temporal compositing, the majority (63.6%) of the clusters have complete spatial coverage from Landsat observations, with the percentage of available pixels ranging from a 5th percentile value of 46.4% to a 95th percentile of 100%.

The delineation of urban and rural areas for SUHI quantification is not trivial. Here we used the Simplified Urban Extent (SUE) algorithm described in Chakraborty and Lee (2019). The SUE algorithm defines the SUHI of an urban cluster as the difference in mean LST of all urban pixels (LST_{urb}) and mean LST of all rural (non-urban and non-water) pixels (LST_{rur}) within the cluster, or:

$$\text{SUHI} = LST_{\text{urb}} - LST_{\text{rur}} \quad (7)$$

By calculating both LST_{urb} and LST_{rur} from pixels within the cluster, the SUE algorithm avoids issues arising from somewhat arbitrary definitions of buffer widths when using commonly used buffer-based rural references (Zhou et al., 2015; Yang et al., 2019; Chakraborty and Lee, 2019). Moreover, not using a buffer around the urban area minimizes the impact of potential differences in atmospheric forcing between the urban core and the rural periphery (Li et al., 2018). This essentially describes the SUHI as a consequence of only the difference in surface climate response of urban and rural areas. The SUE method compares well against both other observational as well as theoretical estimates

of SUHI (Niu et al., 2020; Manoli et al., 2020).

The SUE algorithm requires land cover datasets that can resolve urban and non-urban pixels within each cluster. The original implementation of the algorithm developed by Chakraborty and Lee (2019) was based on 1 km resolution
240 MODIS Terra and Aqua measurements (Wan et al., 2006), with the urban and rural land cover resolved using the 500 m MODIS land cover product (Strahler, 1999). Since both Landsat 5 and ASTER GEDv3 are at finer resolutions, we need suitable higher resolution datasets. To resolve urban pixels, we used one of the highest resolution global urban land cover products currently available, the
245 Global Urban Footprint (GUF) dataset (Esch et al., 2017), which is available at 12 m resolution. The GUF dataset is generated by an automated unsupervised classification scheme using over 180,000 high resolution (3 m) radar images from 2011 and 2012 and shows an overall accuracy of 85% compared to absolute ground truth data. We use Landsat 5 for calculating LST since the only other
250 Landsat product available for the years of validity of the GUF dataset, Landsat 7, has data gaps due to failure of the Scan Line Corrector (SLC), which limits its use. For calculating both LST_{urb} and LST_{rur} , water pixels were first removed based on the Joint Research Center (JRC) 30 m global surface water dataset (Pekel et al., 2016). All remaining GUF pixels within the urban clusters were
255 then used to calculate LST_{urb} . Similarly, for LST_{rur} , we considered all non-GUF and non-water pixels within each urban cluster.

Our final units of calculation are the urban clusters, each of which have summertime and wintertime values of SUHI from ASTER emissivity ($SUHI_{ASTER}$) and the NDVI-based emissivity ($SUHI_{NDVI}$), as well as the intermediate variables, including $LST_{urb,ASTER}$, $LST_{urb,NDVI}$, $LST_{rur,ASTER}$, $LST_{rur,NDVI}$, $\varepsilon_{urb,ASTER}$,
260 $\varepsilon_{urb,NDVI}$, $\varepsilon_{rur,ASTER}$, and $\varepsilon_{rur,NDVI}$. We also include the corresponding variables for the prescribed ε values of 0.88 to 1. Since the native resolution of Landsat 5 TIR is 120 m, ASTER is 90 m, GUF is 12 m, and JRC surface water is 30 m, all calculations for spatial averaging are done after re-gridding all
265 products to 60 m using nearest neighbor resampling.

2.4. Comparison with MODIS Data

Almost all past multi-city studies on the SUHI have used MODIS 1 km LST observations (Zhang et al., 2010; Peng et al., 2011; Clinton and Gong, 2013; Chakraborty and Lee, 2019; Yao et al., 2019; Chakraborty et al., 2020). This is
270 both due to the more frequent return period of MODIS compared to Landsat, which helps with cloud screening (Hu and Brunsell, 2013), and the availability of nighttime values, thus allowing inferences about diurnal patterns. Since here we provide global estimates of SUHI based on different ε assumptions, it is important to compare these estimates with MODIS-based values. We calculate
275 the SUHI using the SUE algorithm using the same urban and rural separation and the MODIS Terra 1 km daytime LST for 2010. MODIS Terra is chosen over Aqua since its equatorial crossing time ($\approx 10:30$ am) is comparable to that for Landsat 5 ($\approx 9:45$ am). The MODIS LST is based on ε values generated from a CBEM approach (Snyder et al., 1998).

280 For this comparison, all analysis is done at a scale of 60 m, identical to the Landsat-based analysis using the same land cover data. This is done to ensure that the differences stem only from the MODIS versus Landsat data. Since the LST estimates from both MODIS and Landsat have uncertainties, we use reduced major axis or geometric mean regression instead of ordinary
285 least square (OLS) regression. Metrics of comparison include the coefficient of determination (r^2) and the mean bias error (MBE) with the MODIS-derived values considered to be the baseline.

2.5. Regions of Interest

In addition to examining the SUHI globally, we separately examine the in-
290 fluence of ε on the the calculated SUHI for each of the five Koppen Geiger climate zones, namely tropical, arid, temperate, boreal, and polar (Rubel and Kottek, 2010). These broad classes divide the Earth’s land surface into regions with large variabilities in vegetation patterns and incoming radiation. Both modeling and observational studies have noted the influence of the background
295 climate on the SUHI intensity (Zhao et al., 2014; Chakraborty and Lee, 2019).

Figure 1a shows the centroids of all the urban clusters and the climate zone they belong to. Note that due to cloud cover or the lack of valid urban or rural pixels within a cluster, we do not get a SUHI value for all the urban clusters in each case. For summer, there are 9041 clusters based on ASTER observations and 300 9011 from the NBEM approach. During winter, there are 8213 clusters from ASTER and 7955 after adjusting by NDVI.

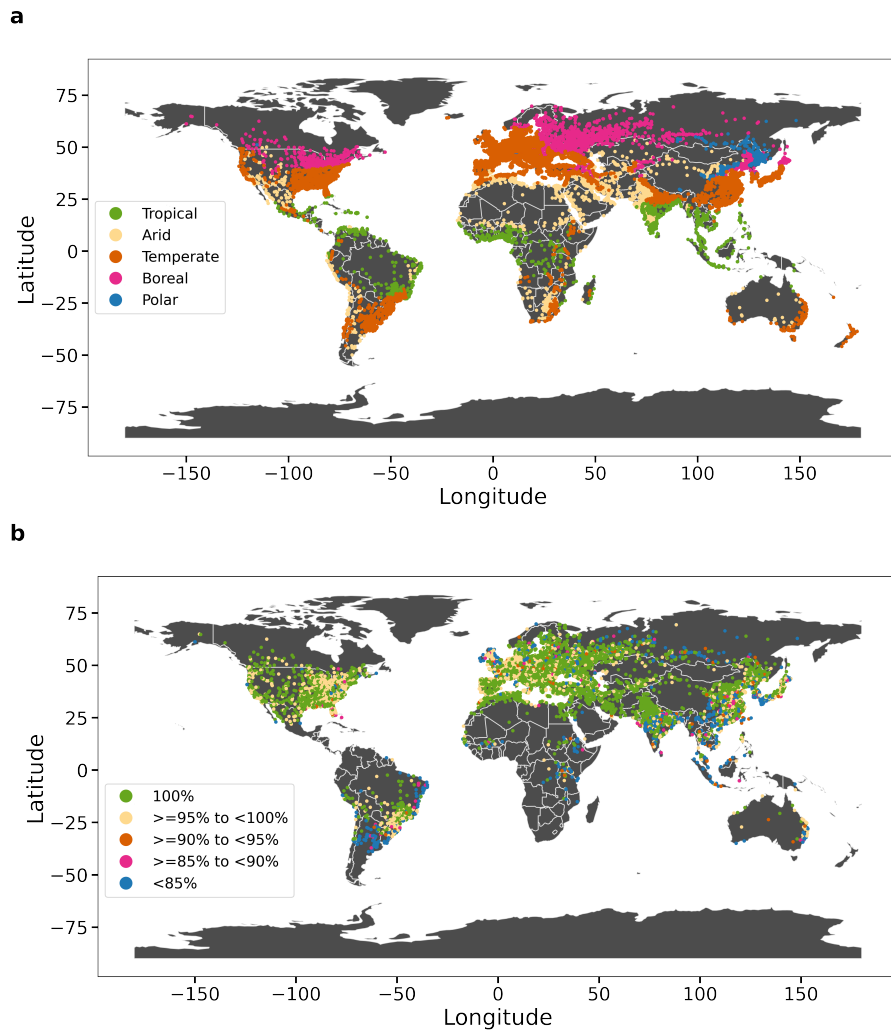


Figure 1: Urban clusters considered in the present study. Sub-figure (a) shows the centroids of every cluster and the climate zones they belong to. Sub-figure (b) shows the percentage of available pixels from the Landsat observations after temporal compositing compared to the maximum number of pixels possible within each cluster during the northern hemisphere summer of 2010.

3. Results

3.1. Emissivity assumptions and urban and rural land surface temperature

Figures 2a and 2b show bar plots of ε_{urb} and ε_{rur} derived using both ASTER
305 data and the NDVI-adjusted approach. Results are shown for both summer
and winter and also divided into each of the Koppen Geiger climate zones.
The ASTER ε_{urb} varies from 0.966 for tropical climate to 0.969 in temperate
climate. For ε_{rur} , there is a slightly higher range of values, with the minimum
value still at 0.966 for tropical climate, but a maximum of 0.971 for temperate
310 climate. Note that the ASTER data are multi-year averages and thus do not
have different values for summer and winter. Both at the global scale and for
most climate zones (except arid), $\varepsilon_{\text{urb,ASTER}}$ is less than $\varepsilon_{\text{rur,ASTER}}$. When
 ε is adjusted using NDVI, we see the variability between the seasons. The
global mean values are higher for summer than for winter ($\varepsilon_{\text{urb,NDVI}} = 0.971$
315 and $\varepsilon_{\text{rur,NDVI}} = 0.975$ for summer; $\varepsilon_{\text{urb,NDVI}} = 0.969$ and $\varepsilon_{\text{rur,NDVI}} = 0.970$ for
winter). In summer, $\varepsilon_{\text{rur,NDVI}}$ varies from 0.969 in arid climate to 0.977 in boreal
climate. Expectedly, $\varepsilon_{\text{urb,NDVI}}$ has less variability, ranging from 0.968 in tropical
climate to 0.972 in boreal climate. For winter, there is less variability, evidently
because vegetation differences between the climate zones, which control this
320 variability, are suppressed. During this season, $\varepsilon_{\text{rur,NDVI}}$ varies from 0.969 in
polar climate to 0.971 in temperate climate and $\varepsilon_{\text{urb,NDVI}}$ varies from 0.968 in
tropical to 0.970 in temperate climate. Overall, ε_{urb} after adjusting for NDVI is
still lower than ε_{rur} . Moreover, particularly for the rural references, the NDVI-
adjusted ε is usually higher than the ASTER observations since vegetation tends
325 to have a higher ε than bare soil.

Figures 2c and 2d show the corresponding daytime LST_{urb} and LST_{rur} using
the two approaches and for the two seasons. The daytime LST values are
evidently driven almost entirely by the energy availability across seasons and
climate zones, with the summer mean daytime LST being highest in arid regions
330 ($\text{LST}_{\text{rur,NDVI}} = 40.59$ °C) and the winter mean daytime LST being lowest in
polar ($\text{LST}_{\text{rur,NDVI}} = -10.64$ °C) and boreal climate ($\text{LST}_{\text{rur,NDVI}} = -9.82$ °C).

Urban areas are not evenly distributed globally, with the majority being in the global north but very few in the high latitudes. This explains why the wintertime mean daytime LST is closer for polar and boreal climate than would be expected
335 for regional means. Tropical areas show the least difference between summer daytime LST ($LST_{\text{rur,NDVI}} = 31.96$ °C) and winter daytime LST ($LST_{\text{rur,NDVI}} = 30.50$ °C) since they do not have strong seasonal cycles. The urban daytime LST values are usually higher than the rural daytime LST values, representing the daytime SUHI intensity. Note that there are some differences between the
340 number of available ε observations from the ASTER multi-year composites and after NDVI adjustment for 2010 due to cloud contamination of the Landsat observations.

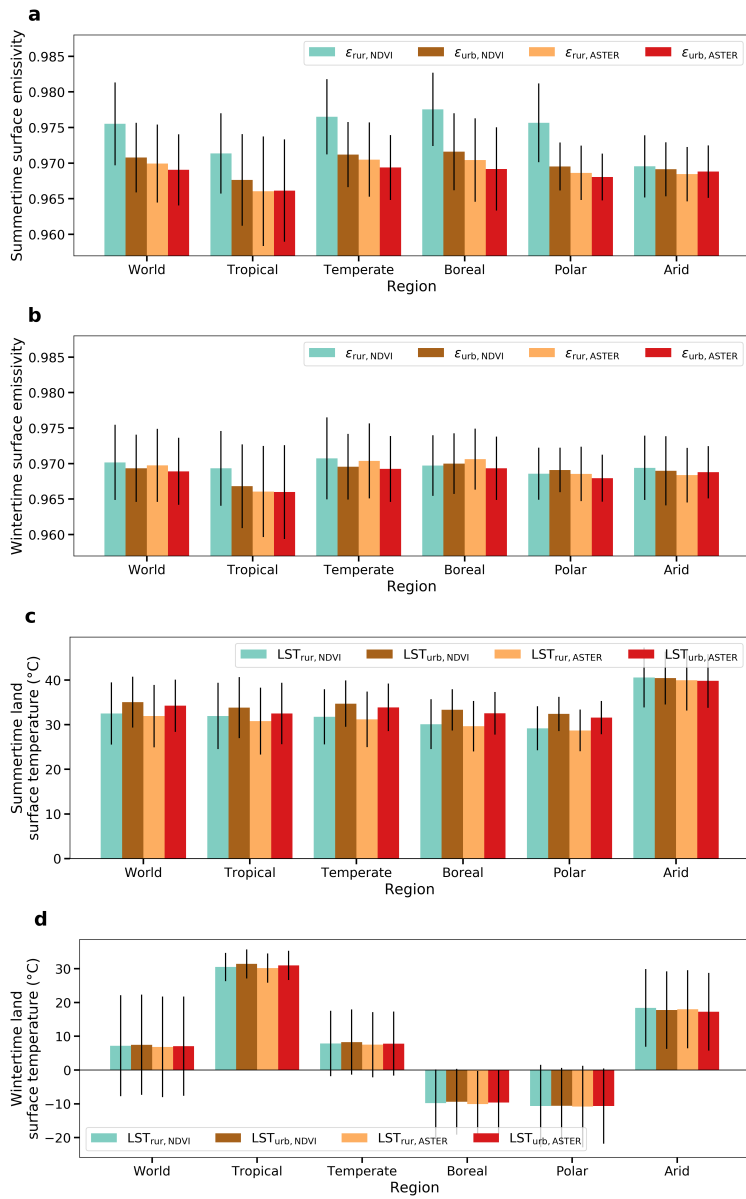


Figure 2: Mean and standard deviation of surface emissivity ((a) and (b)) and daytime land surface temperature ((c) and (d)) for all urban and rural clusters and for each climate zone. Values are shown separately for summer and winter for both the ASTER-based and NDVI-adjusted methods.

3.2. Emissivity and the Surface Urban Heat Island

Figure 3 shows the impact of the ε assumption on the daytime SUHI intensity. The global estimates and the climate zone means are shown along with the percentage difference between the two estimates. Note that the percentage difference in LST depends on the unit used since LST units have different scales. However, this issue disappears when calculating the percentage changes in SUHI since the values are always subtracted from a rural reference in the same temperature scale. Regardless, it is important to be careful when examining percentage changes in variables like SUHI, which have a low signal. To avoid uncertainties arising from sampling differences, we only use the urban clusters for which we get daytime SUHI estimates from both methods. This leaves 9011 clusters during summer and 7955 during winter. During summer, the daytime SUHI is highest for polar climate ($\text{SUHI}_{\text{ASTER}} = 2.89 \text{ }^\circ\text{C}$; $\text{SUHI}_{\text{NDVI}} = 3.21 \text{ }^\circ\text{C}$) and lowest for arid climate ($\text{SUHI}_{\text{ASTER}} = -0.12 \text{ }^\circ\text{C}$; $\text{SUHI}_{\text{NDVI}} = -0.14 \text{ }^\circ\text{C}$), with a global mean of $2.31 \text{ }^\circ\text{C}$ ($\text{SUHI}_{\text{ASTER}}$) to $2.54 \text{ }^\circ\text{C}$ ($\text{SUHI}_{\text{NDVI}}$). For winter, the global mean daytime SUHI ranges from $0.24 \text{ }^\circ\text{C}$ ($\text{SUHI}_{\text{ASTER}}$) to $0.29 \text{ }^\circ\text{C}$ ($\text{SUHI}_{\text{NDVI}}$), with the lowest SUHI seen for arid urban clusters ($\text{SUHI}_{\text{ASTER}} = -0.74 \text{ }^\circ\text{C}$; $\text{SUHI}_{\text{NDVI}} = -0.63 \text{ }^\circ\text{C}$). Tropical urban clusters show the highest winter daytime SUHI ($\text{SUHI}_{\text{ASTER}} = 0.74 \text{ }^\circ\text{C}$; $\text{SUHI}_{\text{NDVI}} = -0.93 \text{ }^\circ\text{C}$). Both seasonal and climatic trends are consistent with previous estimates (Clinton and Gong, 2013; Zhao et al., 2014; Chakraborty and Lee, 2019).

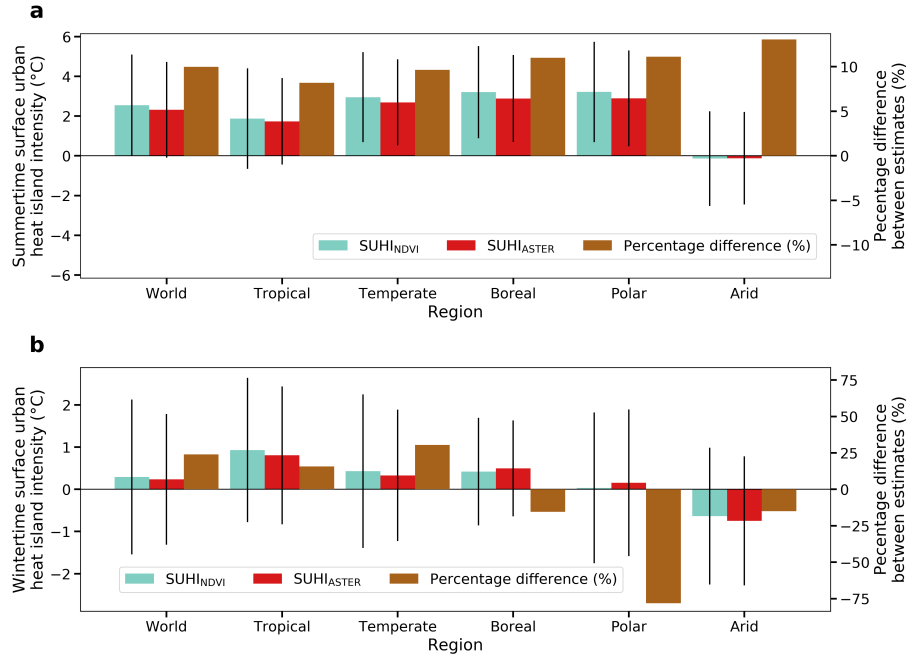


Figure 3: Mean and standard deviation of daytime surface urban heat island intensity based on both the ASTER-based and NDVI-adjusted surface emissivity (ϵ) assumptions for (a) summer and (b) winter. Percentage changes in estimated value when switching from ASTER to NDVI-based ϵ is shown on the right y axis.

The SUHI derived from NDVI-adjusted estimates of ϵ are generally higher since the $\Delta\epsilon$ increases when vegetation is considered (Fig. 2). This is particularly true for summer, with SUHI increasing in magnitude by 8.2% in tropical urban clusters to 13.1% in arid clusters. Globally, the summertime increase in daytime SUHI is around 10% when moving from ASTER ϵ to NDVI-adjusted ϵ . For winter, there is more variability in both magnitude and direction of percentage change, though this is partly driven by the baseline SUHI already being low. The global percentage increase in magnitude is 23.9%, with an increase of 30.4% in temperate urban clusters. Boreal, polar, and arid urban clusters show a decrease in SUHI when the NDVI-adjusted ϵ is used by 15.4%, 78.1%, and 15.0%, respectively.

375 *3.3. Global Spatial Patterns of Surface Urban Heat Island*

Figures 2 and 3 show bulk patterns (mean \pm standard deviation). Since the urban cluster-level information, including their location, are important, we also show the spatial plots of the urban locations and then SUHI intensity using the different methods (Fig. 4). Here we only use the common urban clusters with data from both methods. The summertime patterns for the climate zones are generally replicated in the global maps, with the lowest, mainly negative values, in arid and semi-arid regions in the Middle East, Saharan Africa, southern US and northern Mexico, central Australia, and South America (Figs 4a and 4b). The rest of the world generally shows a positive SUHI intensity. India shows a mixed pattern, with western and central parts showing negative values and northern and southern edges showing positive SUHI, which is consistent with the summer daytime patterns found in Kumar et al. (2017). Overall, the urban cluster mean SUHI intensity during summer calculated after NDVI adjustment varies between a 5th percentile value of -2.16 °C (-2.12 °C for $SUHI_{ASTER}$) to a 95th percentile of 6.07 °C (5.57 °C for $SUHI_{ASTER}$). As also seen in the earlier subsection, the range of daytime SUHI during winter is smaller (5th percentile of -2.05 °C to 95th percentile of 2.39 °C for $SUHI_{NDVI}$; -2.09 to 2.15 °C for $SUHI_{ASTER}$). The contrast between urban clusters in dry versus other climate zones is still apparent, though the positive SUHI values are less extreme.

380

385

390

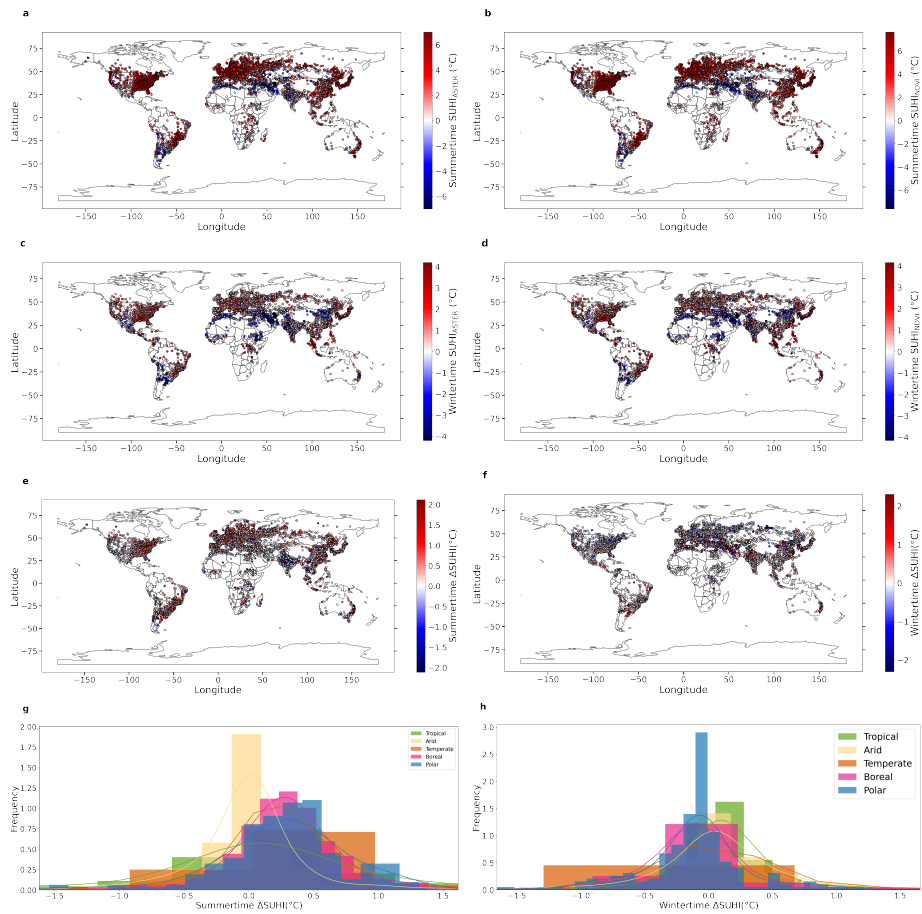


Figure 4: Location of urban clusters and their daytime surface urban heat island intensity (SUHI) estimated using two methods of prescribing surface emissivity from Landsat for summer ((a) and (b)) and winter ((c) and (d)). Sub-figures (e) and (f) show the the urban cluster level difference in estimated SUHI between the two methods for summer and winter, respectively. Sub-figures (g) and (h) show the distribution of these differences during summer and winter for each climate zone.

395 We also examine how using ϵ_{NDVI} instead of ϵ_{ASTER} influences the SUHI by calculating the difference in SUHI (ΔSUHI) between the two methods (Figs 4e and 4f). Although the overall ΔSUHI is positive, there is a range of values. During summer, ΔSUHI ranges from a 5th percentile of -0.59 °C to a 95th percentile of 1.12 °C and during winter, it ranges from -0.77 to 0.98 °C. Interestingly,

400 many of the urban clusters that show a positive ΔSUHI during summer show
a negative anomaly during winter. This includes urban clusters over Europe,
northeast US, and parts of northern China. Similarly, urban clusters over India,
a few over the Amazon, and parts of southeast Asia show positive ΔSUHI values
during winter and negative values during summer. This is consistent with the
405 patterns seen in Fig. 3b, with tropical and temperate urban clusters showing a
percentage increase in winter daytime SUHI when using NDVI-adjusted ε and
boreal, polar, and arid urban clusters showing a percentage decrease in mag-
nitude. We also show the density plots of ΔSUHI during summer and winter
(Figs 4g and 4h). Overall, the differences between two methods is closest to zero
410 for urban clusters in arid climate during summer and for polar urban clusters
in winter. Overall, the positive differences between $\varepsilon_{\text{NDVI}}$ and $\varepsilon_{\text{ASTER}}$ are most
pronounced in tropical areas.

3.4. Comparison with MODIS

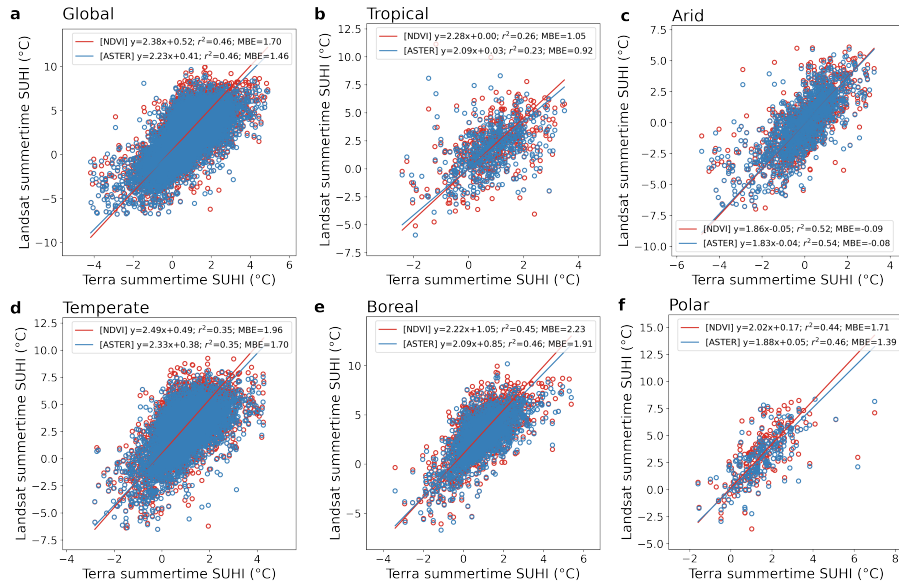


Figure 5: Scatterplots of Landsat versus MODIS-derived daytime summer surface urban heat island intensities for (a) all clusters and for each climate zone, namely (b) tropical, (c) arid, (d) temperate, (e) boreal, and (f) polar. Each point represents one cluster and the equations for the lines of best fit, the coefficients of determination, and the mean bias errors between the two estimates are annotated. The global sample size is 8922, with 480, 1183, 5058, 2005, and 202 clusters lying in the tropical, arid, temperate, boreal, and polar climate zones, respectively.

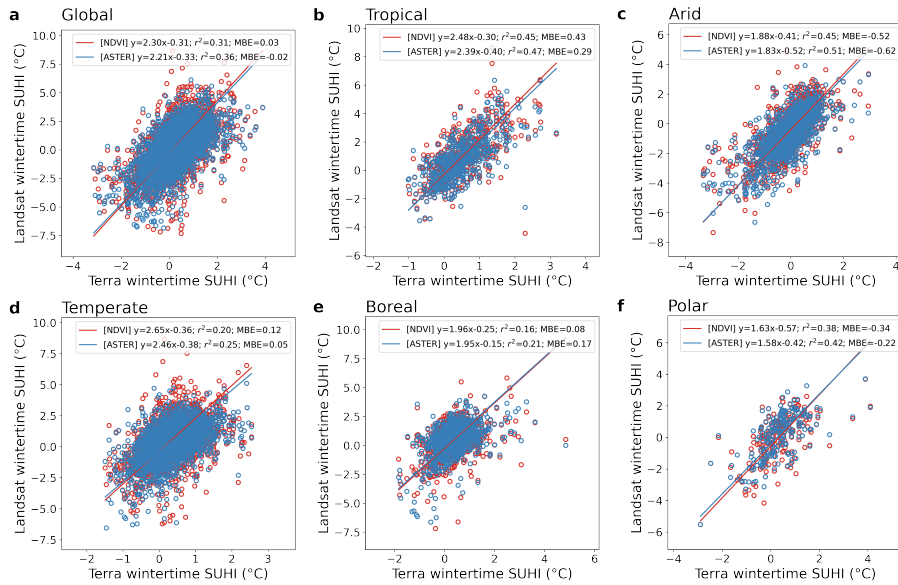


Figure 6: Scatterplots of Landsat versus MODIS derived daytime winter surface urban heat island intensities for (a) all clusters and for each climate zone, namely (b) tropical, (c) arid, (d) temperate, (e) boreal, and (f) polar. Each point represents one cluster and the equations for the lines of best fit, the coefficients of determination, the mean bias errors between the two estimates are annotated. The global sample size is 7911, with 609, 1174, 4312, 1583, and 201 clusters lying in the tropical, arid, temperate, boreal, and polar climate zones, respectively.

We compare our Landsat-derived estimates of daytime SUHI from both
 415 methods with the MODIS Terra-derived estimates, both globally, and for each
 climate zone. The scatter plots, where each point represents the daytime SUHI
 for one urban cluster, are shown for summer (Fig. 5) and winter (Fig. 6). The
 plots show the lines of best fit and the metrics of evaluation and the sample
 sizes for each case are in the figure captions. Overall, the Landsat-derived day-
 420 time SUHI estimates show a moderately strong positive relationship with the
 MODIS-derived estimates during summer (global $r^2 = 0.46$ for both $SUHI_{NDVI}$
 and $SUHI_{ASTER}$), and a somewhat weaker relationship during winter (global r^2
 $= 0.31$ for $SUHI_{NDVI}$ and 0.36 for $SUHI_{ASTER}$). In all cases other than for summer
 in tropical areas, the r^2 values between MODIS and $SUHI_{ASTER}$ is greater

425 than equal to that with $SUHI_{NDVI}$. For the summer, the r^2 values are high-
est for arid urban clusters ($r^2 = 0.52$ for $SUHI_{NDVI}$ and 0.54 for $SUHI_{ASTER}$)
and lowest for tropical urban clusters ($r^2 = 0.26$ for $SUHI_{NDVI}$ and 0.23 for
 $SUHI_{ASTER}$; Fig. 5). This is unsurprising since, even after choosing only clear-
sky pixels, the data availability due to the difference in cloud cover between
430 the two satellites, driven by the distinct return periods, would be higher over
tropical areas and lowest over arid regions (Chakraborty et al., 2020) (see Dis-
cussion). During winter, r^2 values are still highest for arid urban clusters (0.45
for $SUHI_{NDVI}$ and 0.51 for $SUHI_{ASTER}$), but lowest in boreal climate (0.16 for
 $SUHI_{NDVI}$ and 0.21 for $SUHI_{ASTER}$; Fig. 6). Unlike most other climate zones,
435 tropical areas show an improved r^2 between MODIS and Landsat SUHI from
summer to winter. This could be because a large fraction of the tropical urban
clusters (Fig. 1) are located in regions with summer monsoon systems, which
enhance precipitation and cloud cover (Zhisheng et al., 2015; Turner et al., 2020)
and thus interfere with satellite observations of LST.

440 During summer, the SUHI calculated from Landsat is higher (in absolute
magnitude) than that from MODIS (Figs 5 and 6). Assuming MODIS to be
the baseline, the MBE is highest for boreal climate zone (2.23 °C for $SUHI_{NDVI}$
and 1.91 °C for $SUHI_{ASTER}$) and lowest for arid urban clusters (-0.09 °C for
 $SUHI_{NDVI}$ and -0.08 °C for $SUHI_{ASTER}$). During winter, the differences are
445 generally lower, with the global MBE of 0.03 °C for $SUHI_{NDVI}$ and -0.02 °C
for $SUHI_{ASTER}$. Among the climate zones, the arid climate shows the greatest
difference between Landsat and MODIS-derived SUHI (mean difference of -0.52
for $SUHI_{NDVI}$ and -0.62 °C for $SUHI_{ASTER}$). Overall, the wintertime SUHI
magnitudes are similar from both satellites although there are large differences
450 in their distributions. These results indicate that the differences in Landsat-
derived SUHI using the two methods for determining ε are minimal compared
with those based on MODIS LST.

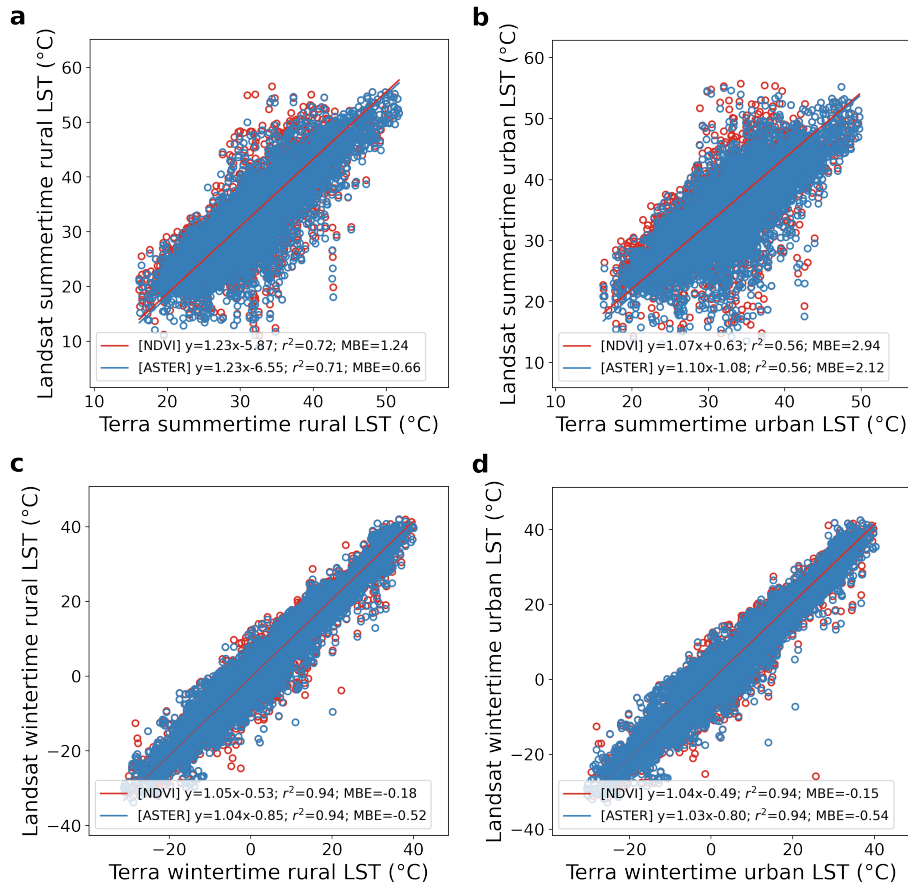


Figure 7: Scatterplots of Landsat versus MODIS-derived daytime rural ((a) and (c)) and urban ((b) and (d)) land surface temperature for all clusters for summer and winter. Each point represents one cluster and the equations for the lines of best fit, the coefficients of determination, the mean bias errors between the two estimates are annotated. During summer, the sample size is 8966 and 8968 for urban clusters and their rural references, respectively. During winter, the sample size is 7921 for both urban clusters and their rural references.

Given the general overestimation in Landsat-derived summer daytime SUHI, it is necessary to check whether this is due to the higher resolution of the
 455 Landsat data which enables better separation of the urban-rural temperature differential or a systematic overestimation in Landsat LST. We examine this by separately evaluating LST_{urb} and LST_{rur} corresponding to all the urban

clusters, shown in Fig. 7. For summer, although LST_{rur} is slightly higher in the Landsat data, particularly after NDVI adjustment of ε_{rur} (MBE = 1.24
460 °C for $LST_{\text{rur,NDVI}}$ and 0.66 °C for $LST_{\text{rur,ASTER}}$), the difference for LST_{urb} is much higher (MBE = 2.94 °C for $LST_{\text{urb,NDVI}}$ and 2.12 °C for $LST_{\text{urb,ASTER}}$). During winter, the Landsat based LST is slightly lower than the MODIS-based value in both urban clusters (MBE = -0.15 °C for $LST_{\text{urb,NDVI}}$ and -0.54 °C for $LST_{\text{urb,ASTER}}$) and their rural references (MBE = -0.18 °C for $LST_{\text{rur,NDVI}}$ and
465 -0.52 °C for $LST_{\text{rur,ASTER}}$). This analysis generally shows that the deviations between MODIS and Landsat LST are not systematic over both urban and rural areas, and that urban areas show additional differences between the two satellites, particularly during summer. This is probably because Landsat data can resolve the thermal signature of urban areas better than MODIS.

470 3.5. Sensitivity Analysis

We estimate the sensitivity of LST_{urb} and LST_{rur} to ε and examined how that would impact SUHI estimates using OLS regressions. Since LST is a linear function of ε in the SMW algorithm (Eq. 3), we get perfect linear relationships in all cases (Fig. 8), with LST decreasing as ε increases. The slope of the lines
475 of best fit give the sensitivity of LST to ε . The sensitivities are pretty similar for LST_{urb} and LST_{rur} for both summer and winter with a value of around -59 °C for a unit change in ε . This linear sensitivity is a consequence of the linear approximation used in the SMW algorithm and is generally valid for the wavelength channel and within the range of temperature we observe on the Earth’s land sur-
480 face. Different algorithms used to estimate LST from satellite observations use different approximations and would yield slightly different sensitivities. If we re-arrange the Stefan–Boltzmann equation (Eq. 2), LST is a power function of ε with a theoretical value of infinity when ε is 0. In contrast, the SMW algorithm shows theoretical temperature values of 92.19 and 64.62 °C for rural surfaces
485 with an ε value of 0 for summer and winter, respectively. When the surface is considered to be a perfect black body, which is somewhat accurate when examining purely vegetated surfaces, the rural and urban reference temperatures

are 30.12 °C and 32.31 °C during summer (4.74 °C and 4.92 °C during winter), respectively. Note here, however, that the Stefan–Boltzmann law is also an
490 approximation, with slight uncertainties associated with the Stefan–Boltzmann constant, deviations from the law seen for high and low temperature regimes, and the assumption of a black body (and by definition, lambertian surfaces) in the derivation of the equation (Baltes, 1973).

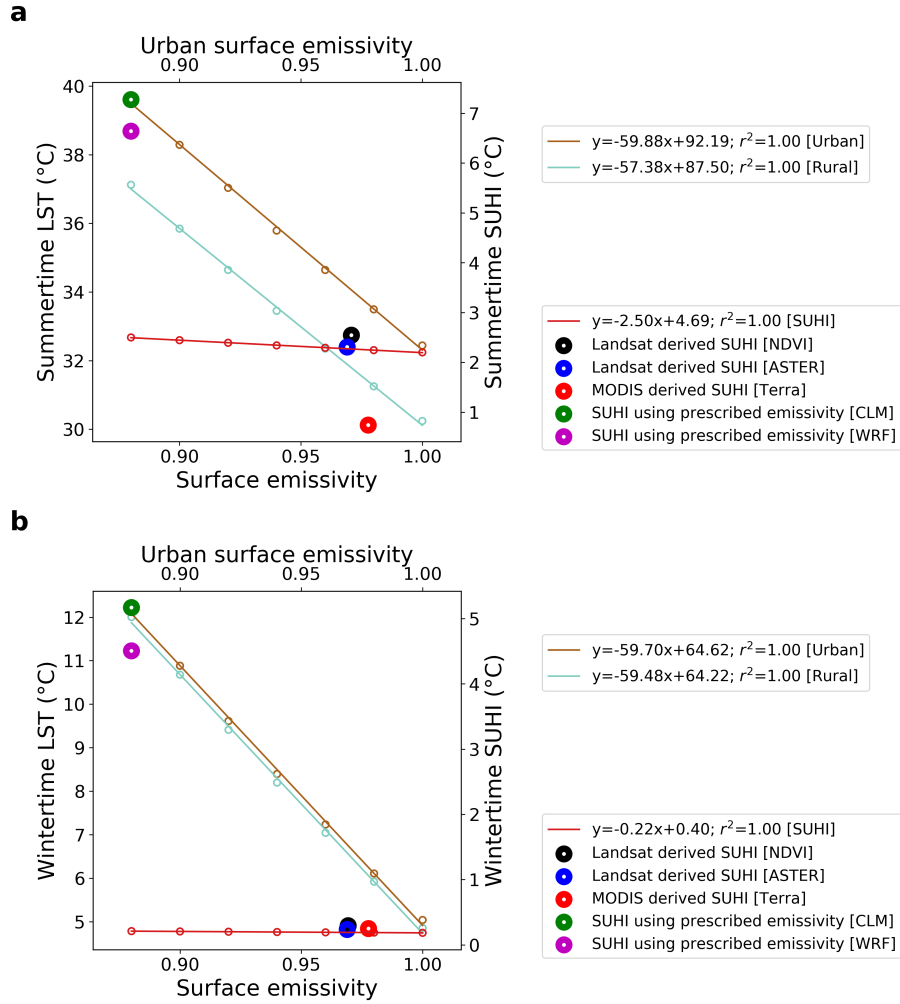


Figure 8: Sensitivity of urban and rural land surface temperature (LST), as well as surface urban heat island intensity (SUHI), to surface emissivity (ϵ) assumptions for **(a)** summer and **(b)** winter days. The temperature sensitivity and SUHI sensitivities correspond to the left and right y-axes, respectively. The global mean values for different assumptions of ϵ , including from ASTER data, after NDVI-adjustment, from MODIS Terra data, and the prescribed ϵ in the Weather Research and Forecasting (WRF) model and Community Land Model (CLM) are provided. The estimates are placed along the top x axis at the corresponding values for urban ϵ , since rural ϵ varies little between these estimates.

The SUHI also decreases with increasing ϵ , with a summer bound of 2.19 °C

495 and a wintertime value of 0.18 °C under the black body assumption for both
urban and rural surfaces. We also show the impact of the prescribed urban
and rural emissivities from ASTER and after NDVI adjustment on the global
SUHI values. As discussed earlier, the lower ε of urban areas compared to their
rural references contributes to the SUHI, with the global mean SUHI being
500 slightly higher after NDVI adjustment (2.54 °C for $SUHI_{NDVI}$ and 2.31 °C for
 $SUHI_{ASTER}$ during summer; 0.29 °C for $SUHI_{NDVI}$ and 0.24 °C for $SUHI_{ASTER}$
during winter). We also plot the global mean SUHI estimates from MODIS
Terra observations, also discussed earlier. Of note, the difference in ε_{urb} between
Landsat and MODIS (global mean average of ε_{urb} in band 31 and 32 = ≈ 0.978
505 for both summer and winter) are minimal and would not explain the higher
SUHI values from Landsat. We also show the impact of the prescribed urban
and rural ε values on simulated SUHI from two commonly used model, the
Weather Research and Forecasting (WRF) Model (Powers et al., 2017) and the
Community Land Model (CLM) (Lawrence et al., 2019). Although there are
510 many models available for simulating urban climate with different assumptions
and parameterizations, a complete survey of the ε assumption in these models
is beyond the scope of the current study. Instead, we provide an illustrative
example from two important cases - with WRF being the mesoscale model used
in the majority of urban climate research in the last decade (Kwok and Ng,
515 2021) and CLM being one of the few operational global climate models with
explicit urban representation (Oleson and Feddema, 2020).

For WRF, we use the prescribed ε for urban land (0.88) and forests (0.95
for coniferous, tropical, and sub-tropical forests) based on the model's land use
lookup table (<https://github.com/NCAR/WRFV3/blob/master/run/LANDUSE.TBL>)
520 to estimate the SUHI from the sensitivities shown in Fig. 8. For CLM, although
 ε varies spatially, for simplicity, we use the values found for North America in
Zhao et al. (2014), which is 0.88 for urban and 0.96 for rural. The theoret-
ical SUHI calculated for the same urban clusters from models if the radiance
differences between urban and rural areas were identical to that derived from
525 the SMW algorithm is much higher than observed values (global mean of 6.64

and 7.27 °C for WRF and CLM, respectively, for summer; 4.50 and 5.17 °C for winter). Although this comparison is simplistic (see Discussion), the lack of agreement between satellite-based ε and model-specified ones, particularly for urban areas, needs to be investigated further for more accurate SUHI estimation and, more broadly, for better constraining urban climate simulations.

4. Discussion

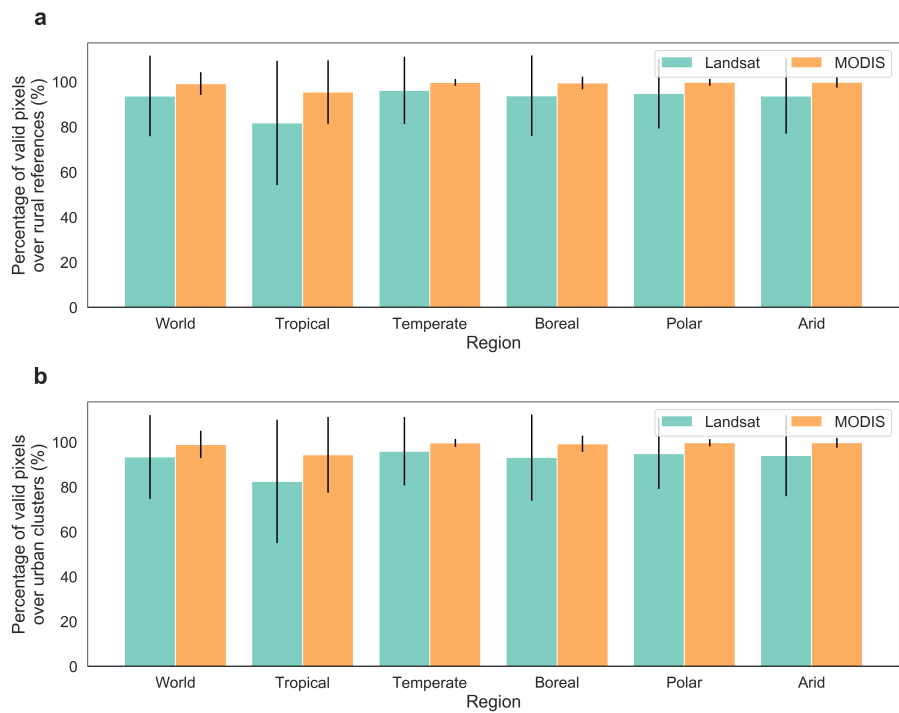


Figure 9: Mean and standard deviation of percentage of available pixels after temporal compositing during northern hemisphere summer from Landsat and MODIS data for all urban clusters (sub-figure (a) is for the rural references and (b) is for the urban references) and for each climate zone.

Unlike MODIS, which has been more frequently used for multi-city comparisons of SUHI, Landsat has a few advantages. The Landsat series has now been operational for over 40 years, with the homogenized Landsat archive being used

535 extensively for high resolution long-term mapping efforts (Liu et al., 2018; Pickens et al., 2020). The Landsat TIR data are available since 1982, which provides an opportunity to study long-term trends in urban temperatures, which is not generally resolved using ground-based observational networks. Moreover, Landsat data being available at a higher resolution than MODIS allows an improved
540 ability to detect thermal hotspots within urban areas. Unfortunately, the major limitation pertains to Landsat’s 16-day return period. The probability of cloud contamination is much higher due to this lower frequency of measurements compared to daily MODIS scenes, particularly relevant for tropical and coastal areas. This is evident when we calculate the percentage of available pixels for
545 the urban and rural references separately from Landsat and MODIS Terra measurements (Fig. 9). As expected, the percentage of available pixels for the urban references is higher for MODIS measurements (global composite mean of 99.2% for MODIS and 93.7% for Landsat). In tropical areas, the difference between the two products is further magnified with the composite mean of the
550 available pixel percentage being 95.4% for MODIS and 81.8% for Landsat. The percentage of available pixels is similar for the rural references (Fig. 9b). Note that the available pixels are calculated here after temporal compositing i.e. at least one pixel is available during the northern hemisphere summer. In reality, Landsat would have a lower number of observations to estimate the pixel-level
555 means, making it hard to compare these observations with more representative clear-sky estimates from MODIS. This lower frequency of measurements matters less for land cover classification since the timescale of land cover changes is usually larger than this return period. However, for dynamic variables like temperature, higher temporal resolution enables us to better constrain clear-sky
560 climatological means, where Landsat would have issues, especially with potential inter-annual variability in cloud cover. To reduce the impact of this noise, we can consider multi-year compositing to define different regimes of SUHI corresponding to each past decade. Although this does reduce the number of data points available to calculate stable long-term trends, this issue will become less
565 important with increasing years of LST data archival. With that being said,

satellite observations from Landsat and MODIS do agree on overall regional patterns in SUHI and can continue to help monitor and provide insights on thermal anomalies associated with urbanization. However, the LST differences between datasets can be of the same order of magnitude as the SUHI signal (see Fig. 7). Previous research has shown that choosing different MODIS-derived products (for instance, MYD11, which uses a split-window algorithm versus MYD21, which uses the ASTER TES algorithm) can lead to differences in SUHI estimates (Yao et al., 2020). The issue is more prevalent for Landsat, which currently lacks a globally available derived product (Yu et al., 2014; Wang et al., 2019). A way forward may be to incorporate ensemble methods to derive uncertainty ranges from multiple datasets and algorithms, thus accounting for differences in sensors, methods, surface emissivity, etc. This is important to consider in future work and can improve our confidence in satellite-based SUHI estimates as we prepare for a warmer and more urbanized future.

Our comparison of the satellite-derived ε with those prescribed in models comes with one major caveat. Since models use broadband ε for longwave radiation, it might be misleading to compare the SUHI calculated using such broadband ε values with the sensitivities found for channel-specific data. To examine further, we calculate broadband emissivities for each urban cluster from the ASTER data using the linear formulation described in Malakar et al. (2018):

$$\varepsilon_{\text{BB}} = c_{10}\varepsilon_{10} + c_{11}\varepsilon_{11} + c_{12}\varepsilon_{12} + c_{13}\varepsilon_{13} + c_{14}\varepsilon_{14} + c_0 \quad (8)$$

where ε_{BB} is the broadband emissivity, ε_{10} , ε_{11} , ε_{12} , ε_{13} , and ε_{14} are the ε values corresponding to channels 10 to 14 of the ASTER GEDv3 dataset, and c_{10} ($=0.014$), c_{11} ($=0.145$), c_{12} ($=0.241$), c_{13} ($=0.467$), c_{14} ($=0.004$) and c_0 ($=0.128$) are empirical coefficients. The distributions of ε_{BB} for urban and rural references, both globally and across climate classes, are shown in Figs 10a and 10b. Overall, urban ε_{BB} is slightly lower than rural ε_{BB} . For rural references, arid regions tend to have the lowest ε_{BB} and boreal regions have the highest. It

is evident that the ASTER-derived ε_{BB} for urban surfaces is higher than the
 595 0.88 considered in CLM or WRF. Since this 0.88 in CLM is a bulk estimate
 of prescribed ε for different urban components, we extracted the grid-level ε
 in the surface dataset used in the latest version of CLM (CLM 5) and show
 their distributions using box and whisker plots (Fig. 10c). The mean urban
 ε_{BB} calculated from ASTER GEDv3 (0.969) is also shown using the horizon-
 600 tal line. In almost all grids, the ε values of the urban sub-components (across
 all urban classes) are lower than the ASTER estimates. Pervious surfaces in
 urban areas are prescribed to have an ε of 0.95. For other sub-components,
 CLM divides the world into 33 regions with their specific urban parameters,
 including ε (Oleson and Feddema, 2020). The values of the ε of roofs in CLM
 605 is particularly low. Unlike CLM, WRF generally uses a single land cover-
 based specification of ε for urban areas. Figure 8 shows the potential SUHI
 value for WRF when run with the slab urban model, which assumes an ur-
 ban ε of 0.88. In WRF with urban canyon representation, urban ε is slightly
 higher and separated into ε values for roofs (0.91), walls (0.91), and roads (0.95;
 610 <https://github.com/NCAR/WRFV3/blob/master/run/URBPARAM.TBL>). Even
 if we assume that half of all urban areas are roads, the SUHI calculated us-
 ing these prescribed emissivities would be higher than Landsat-derived values
 (global summer daytime mean of 3.5 °C versus 2.54 °C for $\text{SUHI}_{\text{NDVI}}$). Since
 these ε are not spatially explicit, some studies using WRF use the ε specification
 615 from CLM (Huang et al., 2021). These sensitivity analyses (Fig. 8) also assume
 that the simulated outgoing longwave from the land components of the models
 would be identical to the values estimated from satellite observations. In reality,
 simulated LST is a function of not just ε , but is strongly modulated by other
 components of the surface energy balance. For CLM, decreases in prescribed ε
 620 have been shown to increase the net radiation and sensible heat flux over urban
 surfaces (Oleson et al., 2008). Given the importance of ε on constraining the
 surface energy budget and the somewhat larger variability in ε expected in urban
 areas, future research should compare the prescribed urban ε and its impacts
 on simulated urban climate across currently operational microscale, mesoscale,

625 and global models.

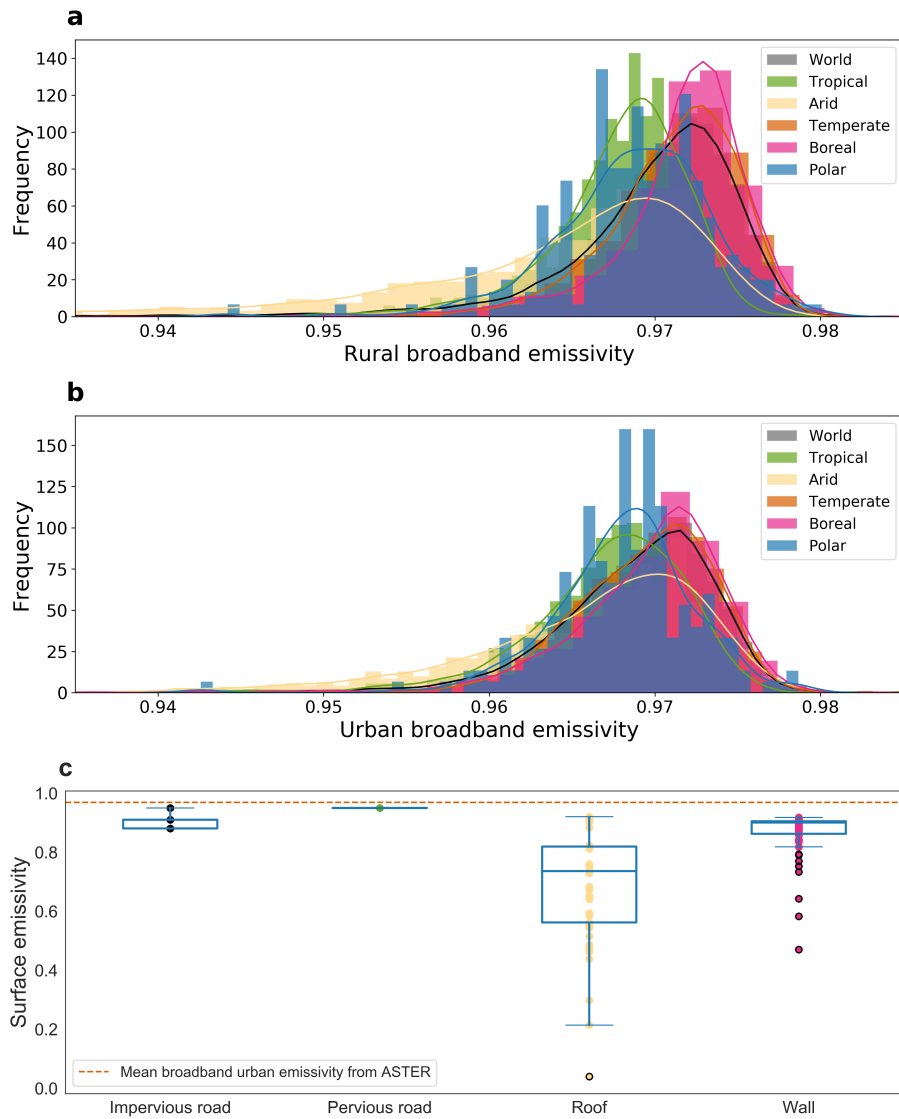


Figure 10: Sub-figures (a) and (b) show the frequency distribution histograms of rural and urban broadband emissivity (ϵ) derived from ASTER data corresponding to all urban clusters and separately for each climate zone. Sub-figure (c) shows box and whisker plots of the prescribed broadband ϵ of all urban sub-components throughout the globe in the latest version of the Community Land Model. The global mean urban broadband ϵ from ASTER is also noted using the horizontal dashed line.

In summary, the assumption of ε can have a strong impact on estimates of urban heat islands, particularly for more vegetated regions. This is true for both satellite observations and numerical models and needs to be benchmarked in a comprehensive manner to improve our representation and understanding of urbanization and its climatic impacts. Although this study uses a sensitivity approach to estimate the impact of ε on SUHI, it should be stressed that the empirical relationships used to estimate LST from TIR data, as well as the methods used to estimate ε , were originally designed for natural surfaces, not urban areas (Van De Griend and Owe, 1993). More importantly, ground-based validation of ε is still rare (Langsdale et al., 2020), and particularly difficult for urban areas due to their heterogeneity. Without such validations, we can expect uncertainties in urban LST and thus, larger noise-to-signal ratios for satellite-derived SUHI. Since Landsat observations allow us to estimate intra-urban variability in SUHI at a higher resolution, an important question is how this ε is affected by the change in surface roughness within urban areas and how that impacts our estimates of spatial LST variability. Finally, when comparing modeled SUHI with satellite observations, it is important to consider the fundamental differences between them. Prescribed ε in models are from material-level ε for broadband thermal radiation, which can be quite low (Artis and Carnahan, 1982). However, most real urban surfaces are not just slabs of constant built-up materials. This introduces difficulties in performing apples-to-apples comparisons between large-scale estimates from satellites and models, since they do not necessarily agree on a common definition for urban areas. With the continued and unprecedented growth in urbanization and given that these technique were initially intended for natural land cover, we need to take a step back to evaluate these methods specifically over urban areas or develop new ones to reduce uncertainties when studying urban climate.

References

- Abrams, M., 2000. The advanced spaceborne thermal emission and reflection
655 radiometer (aster): data products for the high spatial resolution imager on
nasa's terra platform. *international Journal of Remote sensing* 21, 847–859.
- Arnfield, A.J., 2003. Two decades of urban climate research: a review of turbu-
lence, exchanges of energy and water, and the urban heat island. *International
journal of climatology* 23, 1–26. Publisher: Wiley Online Library.
- 660 Artis, D.A., Carnahan, W.H., 1982. Survey of emissivity variability in thermog-
raphy of urban areas. *Remote sensing of Environment* 12, 313–329.
- Baltes, H., 1973. Deviations from the stefan boltzmann law at low temperatures.
Applied physics 1, 39–43.
- Bonafoni, S., Anniballe, R., Pichierri, M., 2015. Comparison between surface
665 and canopy layer urban heat island using MODIS data, in: 2015 Joint Urban
Remote Sensing Event (JURSE), IEEE. pp. 1–4.
- Carlson, T.N., Arthur, S.T., 2000. The impact of land use—land cover changes
due to urbanization on surface microclimate and hydrology: a satellite per-
spective. *Global and planetary change* 25, 49–65.
- 670 Carlson, T.N., Ripley, D.A., 1997. On the relation between ndvi, fractional
vegetation cover, and leaf area index. *Remote sensing of Environment* 62,
241–252.
- Chakraborty, T., Hsu, A., Manya, D., Sheriff, G., 2019a. Disproportionately
higher exposure to urban heat in lower-income neighborhoods: a multi-city
675 perspective. *Environmental Research Letters* 14, 105003. URL: [https://
iopscience.iop.org/article/10.1088/1748-9326/ab3b99](https://iopscience.iop.org/article/10.1088/1748-9326/ab3b99), doi:10.1088/
1748-9326/ab3b99.
- Chakraborty, T., Hsu, A., Manya, D., Sheriff, G., 2020. A spatially explicit
surface urban heat island database for the united states: Characterization,

680 uncertainties, and possible applications. *ISPRS Journal of Photogrammetry and Remote Sensing* 168, 74–88.

Chakraborty, T., Lee, X., 2019. A simplified urban-extent algorithm to characterize surface urban heat islands on a global scale and examine vegetation control on their spatiotemporal variability. *International Journal of Applied Earth Observation and Geoinformation* 74, 269–280. URL: <https://linkinghub.elsevier.com/retrieve/pii/S0303243418304653>, doi:10.1016/j.jag.2018.09.015.

Chakraborty, T., Sarangi, C., Krishnan, M., Tripathi, S.N., Morrison, R., Evans, J., 2019b. Biases in model-simulated surface energy fluxes during the indian monsoon onset period. *Boundary-Layer Meteorology* 170, 323–348.

Chakraborty, T., Sarangi, C., Tripathi, S.N., 2016. Understanding diurnality and inter-seasonality of a sub-tropical urban heat-island. *Boundary-Layer Meteorology* Publisher: Springer.

Chen, F., Yang, S., Su, Z., Wang, K., 2016. Effect of emissivity uncertainty on surface temperature retrieval over urban areas: Investigations based on spectral libraries. *ISPRS journal of photogrammetry and remote sensing* 114, 53–65.

Clinton, N., Gong, P., 2013. Modis detected surface urban heat islands and sinks: Global locations and controls. *Remote Sensing of Environment* 134, 294–304.

Dash, P., Göttsche, F.M., Olesen, F.S., Fischer, H., 2002. Land surface temperature and emissivity estimation from passive sensor data: Theory and practice-current trends. *International Journal of remote sensing* 23, 2563–2594.

705 Duguay-Tetzlaff, A., Bento, V.A., Göttsche, F.M., Stöckli, R., Martins, J., Trigo, I., Olesen, F., Bojanowski, J.S., Da Camara, C., Kunz, H., 2015. Me-

teosat land surface temperature climate data record: Achievable accuracy and potential uncertainties. *Remote Sensing* 7, 13139–13156.

710 Ermida, S.L., Soares, P., Mantas, V., Göttsche, F.M., Trigo, I.F., 2020. Google earth engine open-source code for land surface temperature estimation from the landsat series. *Remote Sensing* 12, 1471.

Esch, T., Heldens, W., Hirner, A., Keil, M., Marconcini, M., Roth, A., Zeidler, J., Dech, S., Strano, E., 2017. Breaking new ground in mapping human settlements from space—the global urban footprint. *ISPRS Journal of Photogrammetry and Remote Sensing* 134, 30–42.
715

Gillespie, A., Rokugawa, S., Matsunaga, T., Cothern, J.S., Hook, S., Kahle, A.B., 1998. A temperature and emissivity separation algorithm for advanced spaceborne thermal emission and reflection radiometer (aster) images. *IEEE transactions on geoscience and remote sensing* 36, 1113–1126.

720 Gorelick, N., Hancher, M., Dixon, M., Ilyushchenko, S., Thau, D., Moore, R., 2017. Google earth engine: Planetary-scale geospatial analysis for everyone. *Remote sensing of Environment* 202, 18–27.

Hook, S.J., Gabell, A.R., Green, A.A., Kealy, P.S., 1992. A comparison of techniques for extracting emissivity information from thermal infrared data
725 for geologic studies. *Remote Sensing of Environment* 42, 123–135.

Hu, L., Brunsell, N.A., 2013. The impact of temporal aggregation of land surface temperature data for surface urban heat island (SUHI) monitoring. *Remote Sensing of Environment* 134, 162–174. Publisher: Elsevier.

Hu, L., Monaghan, A., Voogt, J.A., Barlage, M., 2016. A first satellite-based
730 observational assessment of urban thermal anisotropy. *Remote sensing of environment* 181, 111–121.

Huang, K., Lee, X., Stone Jr, B., Knievel, J., Bell, M.L., Seto, K.C., 2021. Persistent increases in nighttime heat stress from urban expansion despite

- heat island mitigation. *Journal of Geophysical Research: Atmospheres*,
735 e2020JD033831.
- Hulley, G.C., Hook, S.J., Abbott, E., Malakar, N., Islam, T., Abrams, M., 2015. The aster global emissivity dataset (aster ged): Mapping earth's emissivity at 100 meter spatial scale. *Geophysical Research Letters* 42, 7966–7976.
- Jiménez-Muñoz, J.C., Sobrino, J.A., 2003. A generalized single-channel method
740 for retrieving land surface temperature from remote sensing data. *Journal of geophysical research: atmospheres* 108.
- Jin, M., Liang, S., 2006. An improved land surface emissivity parameter for land surface models using global remote sensing observations. *Journal of Climate* 19, 2867–2881.
- 745 Kumar, R., Mishra, V., Buzan, J., Kumar, R., Shindell, D., Huber, M., 2017. Dominant control of agriculture and irrigation on urban heat island in india. *Scientific reports* 7, 1–10.
- Kwok, Y.T., Ng, E.Y.Y., 2021. Trends, topics, and lessons learnt from real case studies using mesoscale atmospheric models for urban climate applications in
750 2000–2019. *Urban Climate* 36, 100785.
- Lagouarde, J.P., Moreau, P., Irvine, M., Bonnefond, J.M., Voogt, J.A., Sollic, F., 2004. Airborne experimental measurements of the angular variations in surface temperature over urban areas: case study of marseille (france). *Remote Sensing of Environment* 93, 443–462.
- 755 Langsdale, M.F., Dowling, T.P., Wooster, M., Johnson, J., Grosvenor, M.J., de Jong, M.C., Johnson, W.R., Hook, S.J., Rivera, G., 2020. Inter-comparison of field-and laboratory-derived surface emissivities of natural and manmade materials in support of land surface temperature (lst) remote sensing. *Remote Sensing* 12, 4127.
- 760 Lawrence, D.M., Fisher, R.A., Koven, C.D., Oleson, K.W., Swenson, S.C., Bonan, G., Collier, N., Ghimire, B., van Kampenhout, L., Kennedy, D., et al.,

2019. The community land model version 5: Description of new features, benchmarking, and impact of forcing uncertainty. *Journal of Advances in Modeling Earth Systems* 11, 4245–4287.
- 765 Li, H., Meier, F., Lee, X., Chakraborty, T., Liu, J., Schaap, M., Sodoudi, S., 2018. Interaction between urban heat island and urban pollution island during summer in berlin. *Science of the total environment* 636, 818–828.
- Li, M., Wang, T., Xie, M., Zhuang, B., Li, S., Han, Y., Song, Y., Cheng, N., 2017. Improved meteorology and ozone air quality simulations using modis
770 land surface parameters in the yangtze river delta urban cluster, china. *Journal of Geophysical Research: Atmospheres* 122, 3116–3140.
- Li, X., Zhou, Y., Yu, S., Jia, G., Li, H., Li, W., 2019. Urban heat island impacts on building energy consumption: A review of approaches and findings. *Energy* 174, 407–419.
- 775 Li, Z.L., Tang, B.H., Wu, H., Ren, H., Yan, G., Wan, Z., Trigo, I.F., Sobrino, J.A., 2013a. Satellite-derived land surface temperature: Current status and perspectives. *Remote sensing of environment* 131, 14–37.
- Li, Z.L., Wu, H., Wang, N., Qiu, S., Sobrino, J.A., Wan, Z., Tang, B.H., Yan, G., 2013b. Land surface emissivity retrieval from satellite data. *International
780 Journal of Remote Sensing* 34, 3084–3127.
- Liu, X., Hu, G., Chen, Y., Li, X., Xu, X., Li, S., Pei, F., Wang, S., 2018. High-resolution multi-temporal mapping of global urban land using landsat images based on the google earth engine platform. *Remote sensing of environment* 209, 227–239.
- 785 Loveland, T.R., Dwyer, J.L., 2012. Landsat: Building a strong future. *Remote Sensing of Environment* 122, 22–29.
- Malakar, N.K., Hulley, G.C., Hook, S.J., Laraby, K., Cook, M., Schott, J.R., 2018. An operational land surface temperature product for landsat thermal

- data: Methodology and validation. *IEEE Transactions on Geoscience and Remote Sensing* 56, 5717–5735.
- 790
- Manoli, G., Fatichi, S., Bou-Zeid, E., Katul, G.G., 2020. Seasonal hysteresis of surface urban heat islands. *Proceedings of the National Academy of Sciences* URL: <https://www.pnas.org/content/early/2020/03/16/1917554117>, doi:10.1073/pnas.1917554117. publisher: National Academy of Sciences eprint: <https://www.pnas.org/content/early/2020/03/16/1917554117.full.pdf>.
- 795
- Marshall, S.J., 1982. We need to know more about infrared emissivity, in: *Thermal Infrared Sensing Applied to Energy Conservation in Building Envelopes*, International Society for Optics and Photonics. pp. 119–128.
- Mitraka, Z., Chrysoulakis, N., Kamarianakis, Y., Partsinevelos, P., Tsochlaraki, A., 2012. Improving the estimation of urban surface emissivity based on sub-pixel classification of high resolution satellite imagery. *Remote Sensing of Environment* 117, 125–134.
- 800
- Mohamed, A.A., Odindi, J., Mutanga, O., 2017. Land surface temperature and emissivity estimation for urban heat island assessment using medium- and low-resolution space-borne sensors: A review. *Geocarto international* 32, 455–470.
- 805
- Muller, C.L., Chapman, L., Grimmond, C.S.B., Young, D.T., Cai, X., 2013. Sensors and the city: a review of urban meteorological networks: SENSORS AND THE CITY. *International Journal of Climatology* 33, 1585–1600. URL: <http://doi.wiley.com/10.1002/joc.3678>, doi:10.1002/joc.3678.
- 810
- Niu, L., Tang, R., Jiang, Y., Zhou, X., 2020. Spatiotemporal patterns and drivers of the surface urban heat island in 36 major cities in china: A comparison of two different methods for delineating rural areas. *Sustainability* 12, 478.
- 815

- Oke, T., 1969. Towards a more rational understanding of the urban heat island. *McGill Climatol Bull* 5, 1–21.
- Oke, T.R., 1982. The energetic basis of the urban heat island. *Quarterly Journal of the Royal Meteorological Society* 108, 1–24. Publisher: Wiley Online Library.
- Oleson, K., Feddema, J., 2020. Parameterization and surface data improvements and new capabilities for the community land model urban (clmu). *Journal of advances in modeling earth systems* 12, e2018MS001586.
- Oleson, K.W., Bonan, G.B., Feddema, J., Vertenstein, M., 2008. An urban parameterization for a global climate model. part ii: Sensitivity to input parameters and the simulated urban heat island in offline simulations. *Journal of Applied Meteorology and Climatology* 47, 1061–1076.
- Pekel, J.F., Cottam, A., Gorelick, N., Belward, A.S., 2016. High-resolution mapping of global surface water and its long-term changes. *Nature* 540, 418–422.
- Peng, S., Piao, S., Ciais, P., Friedlingstein, P., Oettle, C., Bréon, F.M., Nan, H., Zhou, L., Myneni, R.B., 2011. Surface urban heat island across 419 global big cities. *Environmental science & technology* 46, 696–703. Publisher: ACS Publications.
- Peres, L.F., DaCamara, C.C., 2005. Emissivity maps to retrieve land-surface temperature from msg/seviri. *IEEE Transactions on Geoscience and Remote Sensing* 43, 1834–1844.
- Pickens, A.H., Hansen, M.C., Hancher, M., Stehman, S.V., Tyukavina, A., Potapov, P., Marroquin, B., Sherani, Z., 2020. Mapping and sampling to characterize global inland water dynamics from 1999 to 2018 with full land-sat time-series. *Remote Sensing of Environment* 243, 111792.
- Powers, J.G., Klemp, J.B., Skamarock, W.C., Davis, C.A., Dudhia, J., Gill, D.O., Coen, J.L., Gochis, D.J., Ahmadov, R., Peckham, S.E., et al., 2017.

- The weather research and forecasting model: Overview, system efforts, and
845 future directions. *Bulletin of the American Meteorological Society* 98, 1717–
1737.
- Quan, J., Zhan, W., Chen, Y., Wang, M., Wang, J., 2016. Time series decompo-
sition of remotely sensed land surface temperature and investigation of trends
and seasonal variations in surface urban heat islands. *Journal of Geophysical*
850 *Research: Atmospheres* 121, 2638–2657.
- Rao, P.K., 1972. Remote sensing of urban” heat islands” from an environmental
satellite. *Bulletin of the American meteorological society* 53, 647–648.
- Ren, H., Liu, R., Qin, Q., Fan, W., Yu, L., Du, C., 2017. Mapping finer-
resolution land surface emissivity using landsat images in china. *Journal of*
855 *Geophysical Research: Atmospheres* 122, 6764–6781.
- Rubel, F., Kottek, M., 2010. Observed and projected climate shifts 1901-2100
depicted by world maps of the köppen-geiger climate classification. *Meteo-
rologische Zeitschrift* 19, 135.
- Schneider, A., Friedl, M.A., Potere, D., 2010. Mapping global urban areas using
860 modis 500-m data: New methods and datasets based on ‘urban ecoregions’.
Remote Sensing of Environment 114, 1733–1746.
- Sellers, P., Mintz, Y., Sud, Y.e.a., Dalcher, A., 1986. A simple biosphere model
(sib) for use within general circulation models. *Journal of Atmospheric Sci-
ences* 43, 505–531.
- 865 Shastri, H., Paul, S., Ghosh, S., Karmakar, S., 2015. Impacts of urbanization on
Indian summer monsoon rainfall extremes. *Journal of Geophysical Research:*
Atmospheres 120, 496–516. Publisher: Wiley Online Library.
- Snyder, W.C., Wan, Z., Zhang, Y., Feng, Y.Z., 1998. Classification-based emis-
sivity for land surface temperature measurement from space. *International*
870 *Journal of Remote Sensing* 19, 2753–2774.

- Sobrino, J.A., Oltra-Carrió, R., Jiménez-Muñoz, J.C., Julien, Y., Soria, G., Franch, B., Mattar, C., 2012. Emissivity mapping over urban areas using a classification-based approach: Application to the dual-use european security ir experiment (desirex). *International Journal of Applied Earth Observation and Geoinformation* 18, 141–147.
875
- Stewart, I.D., 2011. A systematic review and scientific critique of methodology in modern urban heat island literature. *International Journal of Climatology* 31, 200–217. Publisher: Wiley Online Library.
- Strahler, A., 1999. Modis land cover product algorithm theoretical basis document (atbd) version 5.0. http://modis.gsfc.nasa.gov/data/atbd/atbd_mod12.pdf.
880
- Tang, R., Li, Z.L., Tang, B., 2010. An application of the ts-vi triangle method with enhanced edges determination for evapotranspiration estimation from modis data in arid and semi-arid regions: Implementation and validation. *Remote Sensing of Environment* 114, 540–551.
885
- Theeuwes, N.E., Barlow, J.F., Teuling, A.J., Grimmond, C.S.B., Kotthaus, S., 2019. Persistent cloud cover over mega-cities linked to surface heat release. *npj Climate and Atmospheric Science* 2, 1–6.
- Turner, A.G., Bhat, G., Martin, G., Parker, D.J., Taylor, C., Mitra, A.K., Tripathi, S.N., Milton, S., Rajagopal, E., Evans, J.G., et al., 2020. Interaction of convective organization with monsoon precipitation, atmosphere, surface and sea: The 2016 incompass field campaign in india. *Quarterly Journal of the Royal Meteorological Society* 146, 2828–2852.
890
- Valor, E., Caselles, V., 1996. Mapping land surface emissivity from ndvi: Application to european, african, and south american areas. *Remote sensing of Environment* 57, 167–184.
895
- Van De Griend, A., Owe, M., 1993. On the relationship between thermal emis-

sivity and the normalized difference vegetation index for natural surfaces. International Journal of remote sensing 14, 1119–1131.

900 Voogt, J., 2007. How researchers measure urban heat islands, in: United States Environmental Protection Agency (EPA), State and Local Climate and Energy Program, Heat Island Effect, Urban Heat Island Webcasts and Conference Calls.

Voogt, J.A., Oke, T., 1998. Effects of urban surface geometry on remotely-sensed surface temperature. International Journal of Remote Sensing 19, 895–920.

Voogt, J.A., Oke, T.R., 2003. Thermal remote sensing of urban climates. Remote sensing of environment 86, 370–384.

Wan, Z., et al., 2006. Modis land surface temperature products users' guide. ICES, University of California .

910 Wang, F., Qin, Z., Song, C., Tu, L., Karnieli, A., Zhao, S., 2015. An improved mono-window algorithm for land surface temperature retrieval from landsat 8 thermal infrared sensor data. Remote sensing 7, 4268–4289.

Wang, L., Lu, Y., Yao, Y., 2019. Comparison of three algorithms for the retrieval of land surface temperature from landsat 8 images. Sensors 19, 5049.

915 Yang, J., Wong, M.S., Menenti, M., Nichol, J., 2015. Modeling the effective emissivity of the urban canopy using sky view factor. ISPRS Journal of Photogrammetry and Remote Sensing 105, 211–219.

Yang, Q., Huang, X., Tang, Q., 2019. The footprint of urban heat island effect in 302 chinese cities: Temporal trends and associated factors. Science of the Total Environment 655, 652–662.

920 Yao, R., Wang, L., Huang, X., Gong, W., Xia, X., 2019. Greening in rural areas increases the surface urban heat island intensity. Geophysical Research Letters 46, 2204–2212.

- 925 Yao, R., Wang, L., Wang, S., Wang, L., Wei, J., Li, J., Yu, D., 2020. A detailed comparison of myd11 and myd21 land surface temperature products in mainland china. *International Journal of Digital Earth* 13, 1391–1407.
- Yu, X., Guo, X., Wu, Z., 2014. Land surface temperature retrieval from landsat 8 tirs—comparison between radiative transfer equation-based method, split window algorithm and single channel method. *Remote sensing* 6, 9829–9852.
- 930 Zhang, P., Imhoff, M.L., Wolfe, R.E., Bounoua, L., 2010. Characterizing urban heat islands of global settlements using modis and nighttime lights products. *Canadian Journal of Remote Sensing* 36, 185–196.
- Zhang, Q., Zhang, M., Zhou, W., Xu, W., Zhang, J., 2019. The influence of different urban and rural selection methods on the spatial variation of urban
935 heat island intensity, in: *IGARSS 2019-2019 IEEE International Geoscience and Remote Sensing Symposium, IEEE*. pp. 4403–4406.
- Zhao, L., Lee, X., Smith, R.B., Oleson, K., 2014. Strong contributions of local background climate to urban heat islands. *Nature* 511, 216–219. Publisher: Nature Publishing Group.
- 940 Zhisheng, A., Guoxiong, W., Jianping, L., Youbin, S., Yimin, L., Weijian, Z., Yanjun, C., Anmin, D., Li, L., Jiangyu, M., et al., 2015. Global monsoon dynamics and climate change. *Annual Review of Earth and Planetary Sciences* 43, 29–77.
- 945 Zhou, D., Zhao, S., Zhang, L., Sun, G., Liu, Y., 2015. The footprint of urban heat island effect in china. *Scientific reports* 5, 1–11.